# INVERSE SCATTERING AND IMAGING USING BROADBAND TIME-DOMAIN DATA

W. C. Chew,[1] W. H. Weedon[1] and M. Moghaddam[2]

[1]Electromagnetics Laboratory
Department of Electrical and Computer Engineering
University of Illinois at Urbana-Champaign
Urbana, IL 61801

[2]Jet Propulsion Laboratory
California Institute of Technology
4800 Oak Grove Drive
Pasadena, CA 91109

*(Invited)*

## INTRODUCTION

In inverse scattering, one attempts to determine the internal profile of an inhomogeneous object from measurement data collected away from the scatterer. For example, inverse scattering may be used to locate and image a possible crack or defect in a civil structure in the field of nondestructive testing. It is also used to generate images of geophysical formations for locating minerals or buried objects such as hazardous wastes. Inverse scattering is used in medical imaging in X-rays as well as ultrasonic or CAT scans. There are also military applications for locating and identifying targets from radar data. Basically, the theory of inverse scattering applies whenever waves are used to probe objects for information about their structure. In addition to obtaining the image of an object, a quantitative description of the scatterer such as its permittivity, velocity, or conductivity profile is also obtainable from inverse scattering methods and can contribute invaluable diagnostic information.

The inverse scattering problem is often quite difficult, especially when wave interactions are present. It is usually non-unique because high spatial frequency portions of the object give rise to evanescent waves that cannot be measured. Hence, high spatial frequency information of the object is often lost. Multiple scattering causes the scattered field to be nonlinearly related to the scatterer. In addition to being non-unique and nonlinear, inverse scattering problems are often ill-posed as well due to limited measurement data available enforced by the problem geometry.[1]

Many methods have been proposed in the past to solve particular classes of inverse scattering problems by making certain underlying assumptions about the object or scattering process. For example, in computed tomography (CT),[2] a ray picture is used whereby it is assumed that waves propagate in straight lines and all diffraction and multiple scattering effects are ignored. Diffraction tomography (DT)[3] takes into account diffraction, but ignores multiple scattering and assumes that the object contrast is small. Many methods such as the Gelfand-Levitan-Marchenko method[1] have been proposed to solve the inverse scattering problem "exactly" for 1-D objects (objects such as layered media with one-dimensional spatial variations). However, to date none of these "exact" methods have been shown to be computationally stable for objects with multidimensional spatial variations. Recently developed nonlinear inverse scattering algorithms take into account both diffraction and multiple scattering effects and are valid for arbitrary multidimensional scattering configurations.[4–30]

Time-domain data is important for inverse scattering for a number of reasons. The first is obviously that the information content available from a transient pulse is usually much greater than that available from CW measurements at a few discrete frequencies. With the added information, the problem is usually better conditioned, or more "well-posed." A second reason is perhaps less widely known. One of the biggest problems with conventional diffraction tomography, especially in the area of medical ultrasound imaging,[10] is the "phase wrapping" problem. When only a few frequencies are used to probe an object, and the object space occupies many wavelengths, phase changes from one period to the next become wrapped and are hence ambiguous. This problem does not exist when transient data is used along with a time-domain inverse scattering algorithm such as the Born iterative method (BIM).[25] Another advantage to using time-domain data is that time gating may be used to eliminate unwanted early-time and late-time arrival signals.

We will review here three nonlinear time-domain inverse scattering scattering algorithms that may be used to reconstruct objects directly from time-domain data. These algorithms are the Born iterative method (BIM).[25] the distorted-Born iterative method (DBIM)[24,29] and local shape function (LSF) methods.[26–29] All three of these algorithms may be implemented using the full received waveform to reconstruct an object profile. Reconstructions using computer simulated data are shown and demonstrate that the time-domain nonlinear inverse scattering methods are capable of achieving super-resolution imaging. Similar results are shown using real data collected from a prototype step frequency radar (SFR) imaging system developed at the University of Illinois.

## BORN ITERATIVE METHOD (BIM) AND DISTORTED-BORN ITERATIVE METHOD (DBIM)

The Born iterative method (BIM) and distorted Born iterative method (DBIM) have been proposed and verified as methods of solving the nonlinear inverse scattering problem for dielectric and conductive scatterers.[17–25] In both the BIM and DBIM, the field internal to the scatterer is computed iteratively using a computational forward scattering solver. The major distinguishing feature between BIM and DBIM, however, is that in the BIM, the Green's function used for the inversion is assumed to be that of a homogeneous medium, while in DBIM the background Green's function is updated at each iteration.

Both BIM and DBIM have been implemented for both CW and transient excitations.[19–25] For the CW case, the recursive aggregate T-matrix algorithm (RATMA)[23] as well as the CG-FFT method[31,32] have been used for the fast forward scattering solver. For the transient case, a finite difference time domain (FDTD) algorithm is usually used as the forward solver.[33] One way of implementating the BIM for transient data[25] is to use a FDTD forward solver to generated the field internal to the object, convert to the field data to the frequency domain, and solve the inverse problem in the frequency domain using the known analytic form for the background Green's function. We will not present this method here. Rather, we shall present below a more general DBIM formulation that may be implemented entirely in the time domain and includes the BIM as a special case.

**BIM and DBIM in the Time Domain**

Consider the two-dimensional (2-D) scattering problem illustrated in Figure 1. A line source of current $J_{z,n}(\boldsymbol{r},t)$ produces the electric field $E_{z,n}(\boldsymbol{r},t)$ that is scattered by a 2-D cylindrical scatterer. We shall use the subscript $n$ to parameterize the transmitter number because generally in an inverse scattering measurement there will be multiple transmitter locations. The scatterer is characterized by the permittivity and conductivity profile $\epsilon(\boldsymbol{r})+\delta\epsilon(\boldsymbol{r})$, $\sigma(\boldsymbol{r})+\delta\sigma(\boldsymbol{r})$ and exists in an inhomogeneous background medium $\epsilon(\boldsymbol{r})$, $\sigma(\boldsymbol{r})$. That is, the scatterer consists of a perturbation $\delta\epsilon(\boldsymbol{r})$, $\delta\sigma(\boldsymbol{r})$ in the inhomogeneous background. In the formulation that follows we shall assume that $\delta\epsilon(\boldsymbol{r})$ and $\delta\sigma(\boldsymbol{r})$ are nonzero only within the support volume $V$ of the scatterer. Hence, the permittivity and conductivity everywhere may be written as $\epsilon(\boldsymbol{r})+\delta\epsilon(\boldsymbol{r})$, $\sigma(\boldsymbol{r})+\delta\sigma(\boldsymbol{r})$. This is known as the 2-D $E_z$-polarization or transverse-magnetic (TM) scattering problem in an inhomogeneous background medium.

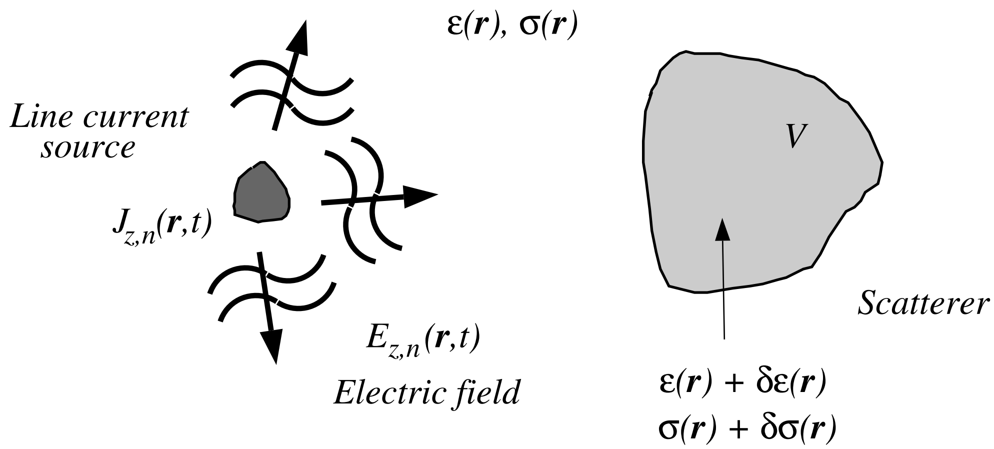


**Figure 1.** Two-dimensional TM scattering problem where the 2-D scatterer $\delta\epsilon(\boldsymbol{r})$, $\delta\sigma(\boldsymbol{r})$ consists of a perturbation of the background inhomogeneous medium $\epsilon(\boldsymbol{r})$, $\sigma(\boldsymbol{r})$. The scatterer is excited by the $\hat{z}$ directed line source of electric current $J_{z,n}(\boldsymbol{r},t)$.

Since both the line source and scatterer in our model have infinite extent in the $\hat{z}$-direction, and are $z$-invariant, the electric field will have only a $\hat{z}$-component. The vertical component of electrical field $E_{z,n}(\boldsymbol{r},t)$ produced by the line source $J_{z,n}(\boldsymbol{r},t)$ is given as the solution to the scalar wave equation

$$\begin{aligned}\left[\nabla^2-\mu_0\epsilon(\boldsymbol{r})\frac{\partial^2}{\partial t^2}-\mu_0\sigma(\boldsymbol{r})\frac{\partial}{\partial t}\right]E_{z,n}(\boldsymbol{r},t)&=\mu_0\frac{\partial}{\partial t}J_{z,n}(\boldsymbol{r},t)\\&+\mu_0\delta\epsilon(\boldsymbol{r})\frac{\partial^2}{\partial t^2}E_{z,n}(\boldsymbol{r},t)+\mu_0\delta\sigma(\boldsymbol{r})\frac{\partial}{\partial t}E_{z,n}(\boldsymbol{r},t)\end{aligned}\tag{1}$$

Under the distorted Born approximation, the solution to the above partial differential equation (PDE) may be written down as

$$E_{z,n}(\boldsymbol{r},t)\approx E_{z,n}(\boldsymbol{r},t)+\delta E^{\epsilon}_{z,n}(\boldsymbol{r},t)+\delta E^{\sigma}_{z,n}(\boldsymbol{r},t).\tag{2}$$

In the above,

$$E_{z,n}(\boldsymbol{r},t)=-\mu_0\int_{-\infty}^{\infty}d\boldsymbol{r}'\int_{-\infty}^{\infty}dt'\;g(\boldsymbol{r},\boldsymbol{r}',t-t')\;\frac{\partial}{\partial t'}J_{z,n}(\boldsymbol{r}',t')\tag{3}$$

is the incident field in the presence of the background inhomogeneous medium $\epsilon(\boldsymbol{r})$, $\sigma(\boldsymbol{r})$. The terms $\delta E^{\epsilon}_{z,n}(\boldsymbol{r},t)$ and $\delta E^{\sigma}_{z,n}(\boldsymbol{r},t)$ are the scattered fields induced by the permittivity perturbation $\delta\epsilon(\boldsymbol{r})$ and conductivity perturbation $\delta\sigma(\boldsymbol{r})$ and are given as

$$\delta E^{\epsilon}_{z,n}(\boldsymbol{r},t)=-\mu_0\int_{-\infty}^{\infty}d\boldsymbol{r}'\int_{-\infty}^{\infty}dt'\;g(\boldsymbol{r},\boldsymbol{r}',t-t')\;\delta\epsilon(\boldsymbol{r}')\frac{\partial^2}{\partial t'^2}E_{z,n}(\boldsymbol{r}',t')\tag{4}$$

and

$$\delta E^{\sigma}_{z,n}(\boldsymbol{r},t) = -\mu_0 \int_{-\infty}^{\infty} d\boldsymbol{r}' \int_{-\infty}^{\infty} dt' \; g(\boldsymbol{r},\boldsymbol{r}',t-t') \; \delta\sigma(\boldsymbol{r}') \; \frac{\partial}{\partial t'} E_{z,n}(\boldsymbol{r}',t'). \tag{5}$$

The inhomogeneous medium Green's function $g(\boldsymbol{r},\boldsymbol{r}',t)$ satisfies

$$\left[\nabla^2 - \mu_0\epsilon(\boldsymbol{r})\frac{\partial^2}{\partial t^2} - \mu_0\sigma(\boldsymbol{r})\frac{\partial}{\partial t}\right] g(\boldsymbol{r},\boldsymbol{r}',t) = -\delta(\boldsymbol{r}-\boldsymbol{r}'). \tag{6}$$

The integral equation given by (2) above is only approximate because the distorted Born approximation[24,29,34] has been used in writing Equations (4) and (5). The approximation amounts to the fact that the incident field $E_{z,n}$ inside integrals in Equations (4) and (5) has been substituted in place of the total field $E_{z,n}$. This approximation is equivalent to assuming that the scattered fields $\delta E^{\epsilon}_{z,n}$ and $\delta E^{\sigma}_{z,n}$ are weak compared to the incident field $E_{z,n}$. The distorted Born approximation also linearizes the integral equation. Note that the BIM algorithm is derivable from DBIM when the inhomogeneous Green's function $g_k(\boldsymbol{r},\boldsymbol{r}',t)$ is replaced by a homogeneous medium green's function.

The distorted Born approximation is used frequently in diffraction tomography to perform inverse scattering on objects with weak contrast compared to a known background. But instead of applying the distorted Born approximation only once, this approximation may be applied repeatedly if the background medium is updated at each step. When the distorted Born approximation is used in an iterative fashion, the resulting algorithm is known as the distorted Born iterative method (DBIM).[20] The solution that is obtained from the DBIM solves the nonlinear inverse problem and hence is valid for much larger contrasts than if the distorted Born approximation were to be applied only once.

In the DBIM, $\epsilon_k(\boldsymbol{r})$ and $\sigma_k(\boldsymbol{r})$ are the permittivity and conductivity at the $k$th iteration. $E_{z,n,k}$ is the incident field at the $k$th iteration in the presence of the background medium $\epsilon_k(\boldsymbol{r})$, $\sigma_k(\boldsymbol{r})$ and are computed numerically using a finite-difference time-domain (FDTD) forward solver. The object model parameters $\epsilon_k(\boldsymbol{r})$, $\sigma_k(\boldsymbol{r})$ may be updated at each iteration using an optimization scheme such as the conjugate gradient method.

Equations (4) and (5) above can be thought of as operator forms of the Fréchet derivatives that map perturbations $\delta\epsilon_k(\boldsymbol{r})$ and $\delta\sigma_k(\boldsymbol{r})$ into the field variations $\delta E^{\epsilon}_{z,n,k}(\boldsymbol{r},t)$ and $\delta E^{\sigma}_{z,n,k}(\boldsymbol{r},t)$. The Fréchet transposed operators corresponding to these Fréchet derivatives map the field perturbations $\delta E^{\epsilon}_{z,n,k}(\boldsymbol{r},t)$ and $\delta E^{\sigma}_{z,n,k}(\boldsymbol{r},t)$ back into the permittivity and conductivity spaces. It can be shown[25,29] that these Fréchet transposed operators are given as

$$\begin{aligned}\delta\epsilon_k(\boldsymbol{r}) = \mu_0 \sum_{n=1}^{N_T} \int_0^T dt \frac{\partial^2}{\partial t^2} E_{z,n,k}(\boldsymbol{r}',T-t) \\ \times \sum_{m=1}^{N_R} \int_0^T dt' \; g_k(\boldsymbol{r}',\boldsymbol{r}_m,t-t') \; \delta E_{z,n,k}(\boldsymbol{r}_m,T-t')\end{aligned} \tag{7}$$

and

$$\begin{aligned}\delta\sigma_k(\boldsymbol{r}) = \mu_0 \sum_{n=1}^{N_T} \int_0^T dt \frac{\partial}{\partial t} E_{z,n,k}(\boldsymbol{r}',T-t) \\ \times \sum_{m=1}^{N_R} \int_0^T dt' \; g_k(\boldsymbol{r}',\boldsymbol{r}_m,t-t') \; \delta E_{z,n,k}(\boldsymbol{r}_m,T-t').\end{aligned} \tag{8}$$

Both the Fréchet derivative and transposed operators are required in a conjugate gradient optimization scheme. The Fréchet derivative operator is used in computing the conjugate gradient step size for update along a given search direction and may be computed with a single call to a FDTD forward solver. The Fréchet transposed operator is used to compute the gradient and hence the search direction and may be computed as a backpropagation followed by a correlation.

### Computer Simulated BIM and DBIM Results

Permittivity reconstructions were generated using computer simulated data for both the BIM and DBIM inversion algorithms. The full-angle bistatic measurement shown in Figure 2 was used to generate the forward scattering data using a FDTD code.

Figure 3 shows a BIM reconstruction of two point objects placed 0.1 wavelength (1 grid point) apart. The permittivity contrast for this case is 2:1. This result illustrates the phenomenon of super-resolution,[22,24,25] where objects separated by less than 0.5 wavelength may be resolved. Figure 4 shows another BIM reconstruction for two cylindrical step discontinuities with a permittivity contrast of 2:1 relative to the background medium. The total object diameter for this case is 8.5 wavelengths. Apparently, "phase wrapping" is not a problem here.

Figure 5 shows a DBIM reconstruction of a smooth permittivity profile with a peak contrast of 10:1 and object diameter 1.5 wavelengths. The original object was nearly identical to the reconstruction here. A reconstruction of this high contrast case was attempted using BIM, but the algorithm did not converge. The DBIM algorithm seems to be capable of inverting much larger contrasts than BIM.

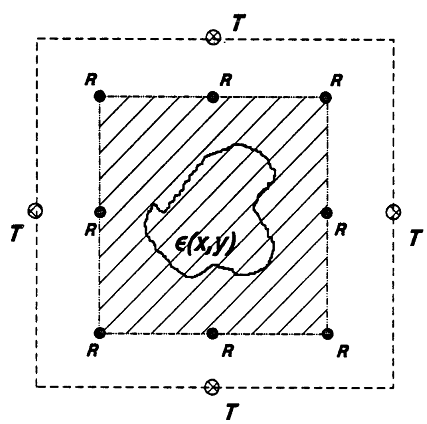


**Figure 2.** Full angle bistatic measurement configuration for BIM and DBIM computer simulations.

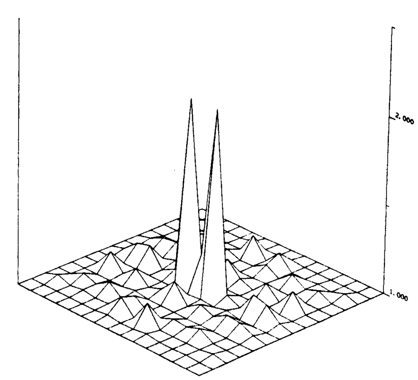

**Figure 3.** BIM reconstruction of two point objects separated by 0.1 wavelengths with a permittivity contrast of 2:1.

## THE LOCAL SHAPE FUNCTION (LSF) METHOD

### LSF Formulation in the Time Domain

The BIM and DBIM work well for dielectric and conductive media with contrasts as great as 10:1. But for metallic scatterers, where the contrast is infinite in theory, the linearizing Born approximations that are applied at each step of the BIM and DBIM may not be valid. Recently, we have developed a new inverse scattering method known as the local-shape-function (LSF) method[26–29] to invert strong metallic scatterers. This technique maps a scatterer with infinite conductivity into a problem with a scatterer described by a binary function which ranges between 0 and 1. By so doing, the extremely nonlinear problem of scattering by a metallic scatterer is mapped into another space where the problem is more linear, but still nonlinear. Eventually, it

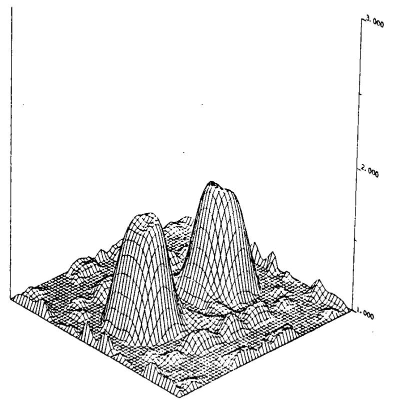

**Figure 4.** BIM reconstruction of two cylindrical step discontinuities with a permittivity contrast of 2:1. The object object size is 8.5 wavelengths.

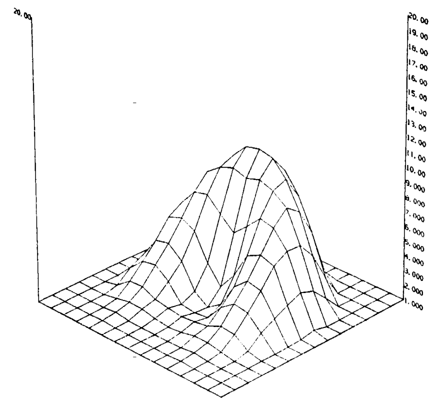

**Figure 5.** DBIM reconstruction of a 10:1 peak permittivity contrast smooth object of diameter 1.5 wavelengths. The original object is nearly identical to the reconstruction.

allows us to iteratively reconstruct metallic scatterers whereas the application of BIM or DBIM would converge extremely slowly or not at all.

Although we have developed LSF theory that applies to both CW and transient excitation, the LSF algorithm is more simply derived in the frequency domain.[26,27] First, the scattering region is discretized by dividing the scattering volume $V$ into $N$ regions occupying volumes $V_i, \quad i = 1, \ldots, N$. Then, a binary shape function $\gamma_i$ is assigned to each volume $V_i$ depending on whether the individual volume contains a metallic scatterer. If $\mathcal{S}$ represents the total volume occupied by metallic scatterers, then we have

$$\gamma_i = \begin{cases} 1, & V_i \bigcap \mathcal{S} \neq \emptyset \\ 0, & V_i \bigcap \mathcal{S} = \emptyset \end{cases} \tag{9}$$

as in Figure 6.

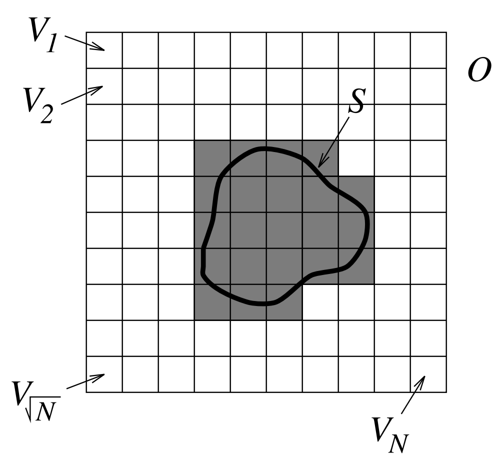


**Figure 6.** Discretization of scattering object volume $\mathcal{O}$ into $N$ subvolumes $V_i, \quad i = 1, \ldots, N$. Surface $S$ indicates the metallic scatterer and the shaded region is where $\gamma_i = 1$.

We now examine how the local shape function may be implemented as a volumetric boundary condition in a FDTD forward solver. Using the FDTD method, a scatterer occupying volume $V$ is discretized into many subvolumes $V_i$ as in Figure 6. We then assume that the scatterer has a homogeneous permittivity and conductivity in each subvolume $V_i$. Metallic scatterers may be implemented in one of two ways. One method is to simply assign a large conductivity value to the cells where $\gamma_i = 1$. Another way to deal with metallic scatterers is to manually enforce the boundary condition that $E_{z,n}(\boldsymbol{r}_i) = 0$ at the locations $\boldsymbol{r}_i$ where $\gamma_i = 1$. This boundary condition can be thought of as placing a filamental metallic scatterer at each location $V_i$ where $\gamma_i = 1$. We call the above a "volumetric boundary condition" because it is applied at arbitrary locations where $\gamma_i = 1$ inside the volume $V$.

Mathematically, the LSF volumetric boundary condition may be written as

$$E_{z,n}(\boldsymbol{r}_i, t) = \left(1 + \gamma_i T_{i(1)}\right) E^{\mathrm{g}}_{z,n}(\boldsymbol{r}_i, t) \tag{10}$$

where $T_{i(1)}$ is the single-scatterer T-matrix. In the case of filamental metallic scatterers, $T_{i(1)} = -1$. Hence, for $\gamma_i = 1$, Equation (10) enforces the boundary condition $E_{z,n}(\boldsymbol{r}_i, t) = 0$. $E^{\mathrm{g}}_{z,n}(\boldsymbol{r}_i, t)$ is the incident field on the scatterer at position $\boldsymbol{r}_i$ that includes multiple scattering effects from other cells $V_j, \quad j \neq i$. We call $E^{\mathrm{g}}_{z,n}(\boldsymbol{r}, t)$ the "ghost field" because it represents the total field that would be produced at $\boldsymbol{r}_i$ assuming $\gamma_i = 0$, or that a metallic scatterer is not present at $\boldsymbol{r}_i$.

Up to this point, we have assumed that $\gamma_i$ represents a binary variable that is either 0 or 1. In a practical iterative optimization scheme, it is necessary to relax this requirement and instead let $\gamma_i$ be a continuous real variable on the interval $[0, 1]$. The inverse scattering algorithm would then produce an image of the variable $\gamma_i$ as a function of 2-D space.

For brevity, we shall not include the details of the T-matrix formulation of the LSF algorithm here, but rather refer the reader to the literature.[29] The time-domain LSF algorithm may be implemented in an iterative algorithm with a structure similar to that of the DBIM algorithm. The major difference between the new LSF algorithm and the DBIM algorithm is that the Fréchet derivative and Fréchet transposed operators are different.

Using the LSF method the Fréchet derivative operator may be written as

$$\delta E_{z,n,k}(\boldsymbol{r}, t) = \int_{-\infty}^{\infty} d\boldsymbol{r}' \int_0^T dt' \; h(\boldsymbol{r}, \boldsymbol{r}', t - t') \; \delta\gamma_k(\boldsymbol{r}') \; E^{\mathrm{g}}_{z,n}(\boldsymbol{r}', t'). \tag{11}$$

where $h(\boldsymbol{r}, \boldsymbol{r}', t)$ is the inhomogeneous medium Green's function in the presence of $\gamma_k(\boldsymbol{r})$. The Fréchet transposed operator may be written as

$$\begin{aligned} \delta\gamma_k(\boldsymbol{r}') = \sum_{n=1}^{N_T} \int_0^T dt \; & E^{\mathrm{g}}_{z,n}(\boldsymbol{r}', T - t) \\ & \times \sum_{m=1}^{N_R} \int_0^T dt' \; h(\boldsymbol{r}', \boldsymbol{r}_m, t - t') \; \delta E_{z,n,k}(\boldsymbol{r}_m, T - t') \end{aligned} \tag{12}$$

In the integral form of the Fréchet derivative and transposed operators above, we have generalized our definition of the local shape function $\gamma_i$ to be a function of the continuous variable $\boldsymbol{r}$.

## Computer Simulated LSF Results

The LSF algorithm was verified by reconstructing computer simulated scattering data obtained from the inverse Fourier transform the output of a two cylinder frequency-domain T-matrix code[1]. The geometry used in the computer simulation results is shown in Figure 7. The scattering object $\mathcal{O}$ was considered to be contained inside a 19.9 cm $\times$ 19.9 cm ($25 \times 25$ grid points) region. The background medium was assumed to be that of free space. The transmitted waveform had a $-3$ dB cutoff of 1.22 GHz, corresponding to a minimum wavelength $\lambda_{\min} = 24.5$ cm.

The scattering data of two metallic scatterers, each of radius $a = .794$ cm ($.0645\lambda_{\min}$) and separated by $d = 11.2$ cm ($.458\lambda_{\min}$) was computed using the analytic formulation. The reconstruction obtained from the LSF method and is shown in Figure 8 and that obtained using the DBIM with a conductivity optimization is shown in Figure 9. No convergent solution was obtainable using DBIM with permittivity optimization. In Figure 8, the two metallic scatterers are easily distinguishable, while those in Figure 9 are not resolved.

The relative residual error (RRE) at the $k$th iteration is defined as

$$\text{RRE} = \left[ \frac{\sum_{n=1}^{N_T} \sum_{m=1}^{N_R} \int_0^T dt \; \left[E_{z,n}(\boldsymbol{r},t) - E_{z,n,k}(\boldsymbol{r},t)\right]^2 \; W(t)}{\sum_{n=1}^{N_T} \sum_{m=1}^{N_R} \int_0^T dt \; \left[E_{z,n}(\boldsymbol{r},t)\right]^2 \; W(t)} \right]^{1/2} \tag{13}$$

where $E_{z,n}(\boldsymbol{r}_m, t)$ is the measured electric field at the $m$th receiver due to the $n$th transmitter, $E_z(\boldsymbol{r}_m, t)$ is the computed solution at the $k$th iteration and $W(t)$ is a time varying gain that is used to to boost the later signal arrivals. The RRE is shown in Figure 10 for each iteration step. Only twenty iteration steps were computed and it is clear from Figure 10 that while both algorithms converged, the LSF algorithm has a much faster convergence that the DBIM with conductivity optimization. The DBIM solution leveled off with a RRE of about (0.5), whereas the LSF solution leveled off at about (0.15).

Figure 11 shows a LSF reconstruction of two metallic scatterers that are of the same radius as those used in Figure 8, but the separation has been reduced to $d = 8.42$ cm ($.344\lambda_{\text{min}}$). The two cylinders are still clearly resolved, but it is apparent that this separation is at about the resolution limit of this algorithm.

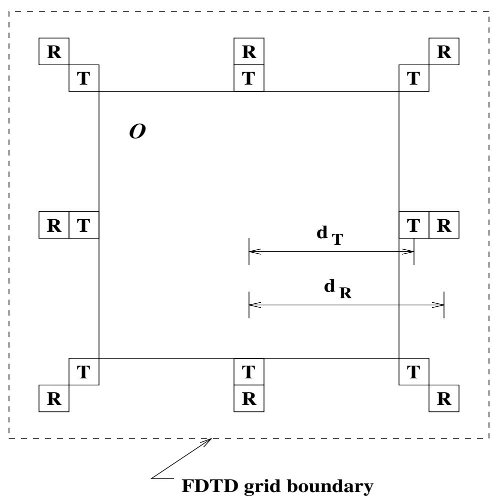


**Figure 7.** Geometry for bistatic inverse scattering simulation. Object region is 19.9 cm × 19.9 cm (25 × 25 grid points), $d_T = 12.7$ cm ($.517\lambda_{\text{min}}$), $d_R = 13.5$ cm ($.549\lambda_{\text{min}}$).

## EXPERIMENTAL RESULTS

A prototype bistatic step-frequency radar (SFR) microwave measurement system was developed at the University of Illinois to collect scattering data. The system operates in the frequency range of 2 – 12 GHz and is intended for nondestructive evaluation applications, including the imaging of defects in civil structures such as bridges and buildings. Although data is collected in the frequency domain, the system we collect data at several (typically 200) evenly spaced frequencies and convert the magnitude and phase data in the frequency domain to a time pulse by means of a Fourier transform. The details of this data collection system will not be shown here, but will be presented in a later paper. However, we will show some results here to demonstrate the effectiveness of our inverse scattering algorithms in a practical imaging system.

The arrangement of transmitters, receivers and the object grid for the experiment is as shown in Figure 12. The measurement consists of 5 transmitter locations

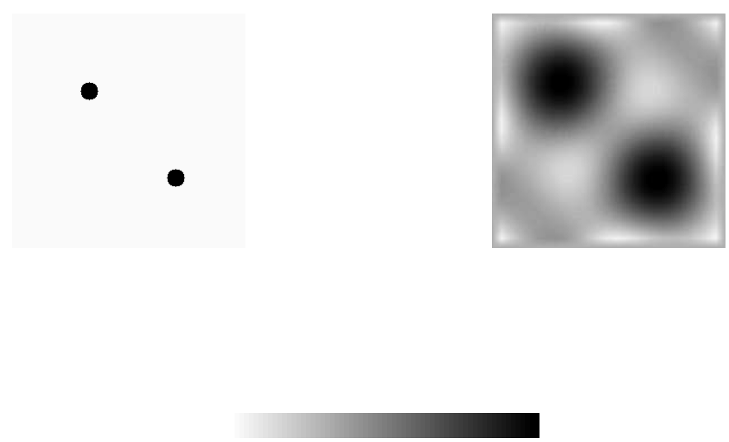


**Figure 8.** Local shape function reconstruction of two metallic cylinders, each of radius $a =$ .794 cm (.0645$\lambda_{\mathrm{min}}$), separation $d = 11.2$ cm (.458$\lambda_{\mathrm{min}}$) using geometry shown in Figure 7. The LSF algorithm was applied to the computer-generated scattering data for 20 iterations.


**Figure 9.** Conductivity reconstruction using the distorted Born iterative method of the same object as used in Figure 8. The DBIM was applied to the computer-generated scattering data for 20 iterations.

indicated by a “T” in Figure 12, and 6 receiver locations indicated by an “R”. For the object functions and reconstructions shown below, the object space consists of the $35 \times 35$ grid point (g.p.) region indicated by a dashed box in Figure 12.

To illustrate the reconstruction of metallic objects and show the horizontal and vertical resolution of our imaging system, two different cases of metallic scattering objects were considered. First, we examined two metallic cylinders aligned horizontally, or parallel to the array. The cylinders were separated by 3.2 cm, each with a diameter of 0.4 cm. The reconstruction is shown in Figure 13 and it is clear that we can resolve this case very well. The second case that we considered consisted of the same cylinders with 3.2 cm separation, but in this case aligned vertically. The reconstruction is shown in Figure 14, and both cylinders are still well resolved.

From an inverse scattering theory point of view, metallic scatterers are more difficult to reconstruct than dielectric scatterers because the inverse problem is more nonlinear. However, from a practical measurement perspective, the reconstruction of dielectric scatterers is more difficult because the scattered field is much weaker from dielectric scatterers and hence the signal-to-noise ratio is lower. To illustrate that

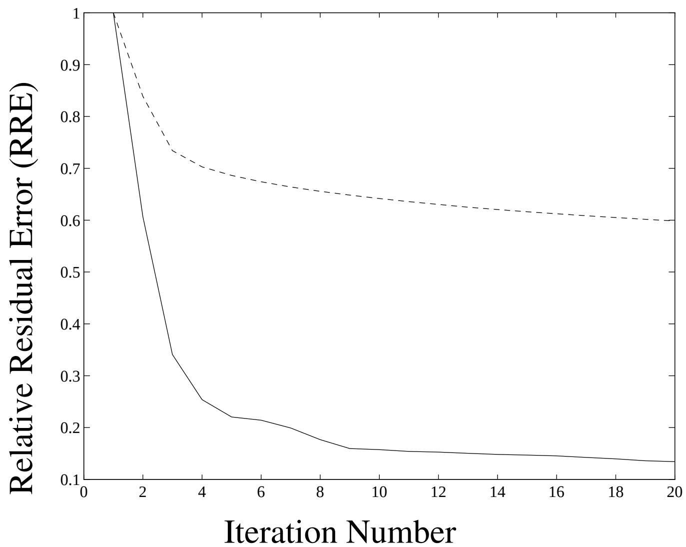


**Figure 10.** Comparison of relative residual error (RRE) for LSF (solid curve) and DBIM (dashed curve) reconstructions shown in Figures 8 and 9 from computer-generated scattering data.

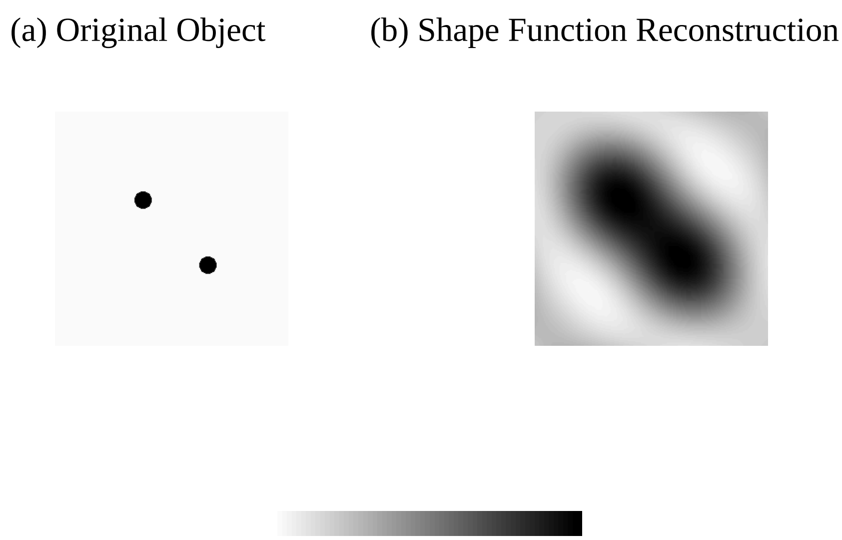


**Figure 11.** Local shape function reconstruction of two metallic cylinders more closely spaced than those shown in Figure 8. Cylinders are of radius $a = .794$ cm ($.0645\lambda_{\min}$), separation $d = 8.42$ cm ($.344\lambda_{\min}$) using geometry shown in Figure 7. The LSF algorithm was applied to the computer-generated scattering data for 20 iterations.

we can also measure dielectic scatterers with our prototype data collection system and generate quality reconstructions, we have collected data from two different sized plastic PVC pipes in air. A reconstruction generated by the DBIM algorithm for a PVC pipe of diameter 2.7 cm in air is shown in Figure 15, and the reconstruction of a PVC pipe of diameter 4.8 cm is shown in Figure 16.

## CONCLUSIONS

We have presented here a review of the Born and distorted-Born iteratitive methods as well as the recently developed local shape function method for nonlinear inverse scattering. We demonstrated that these nonlinear inverse scattering algorithms are capable of achieving super-resolution imaging, and can distinguish objects separated by less than 0.5 wavelengths. These time domain algorithms avoid many ill-conditioning

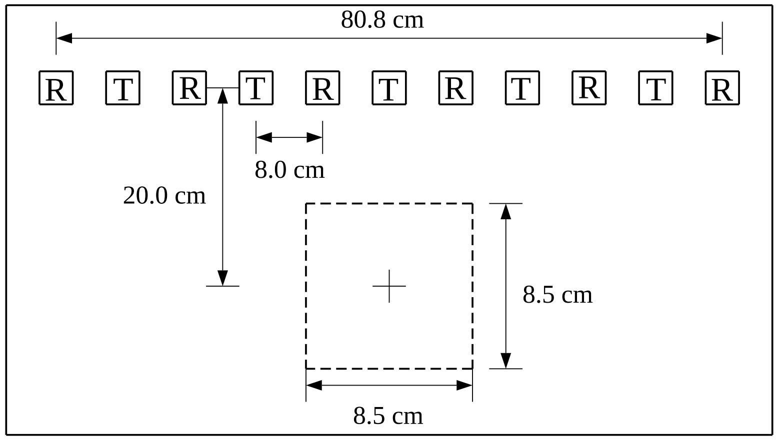


**Figure 12.** Arrangement of transmitters, receivers and object grid experimental data collection. (Note: drawing not to scale).

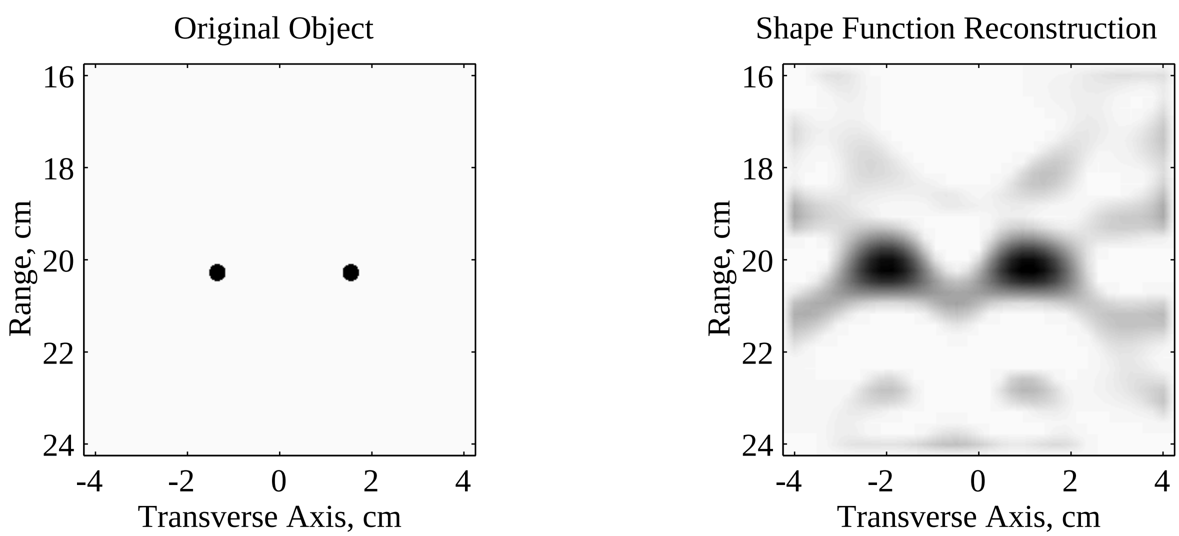


**Figure 13.** Experimental data reconstruction showing original object and LSF reconstruction of two metallic cylinders of diameter 0.4 cm aligned horizontally with separation 3.2 cm.

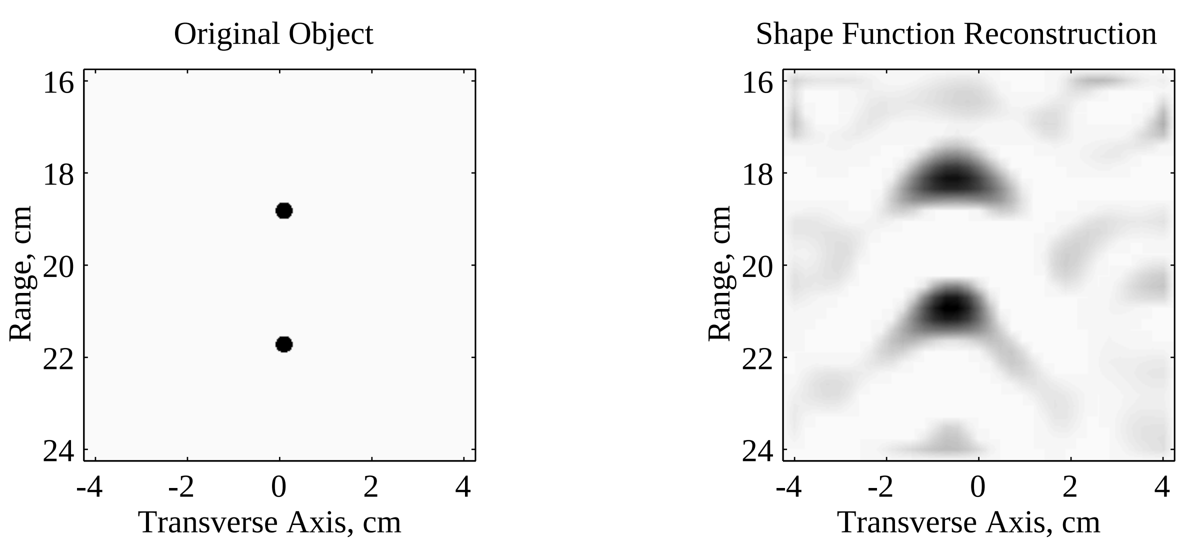


**Figure 14.** Experimental data reconstruction showing original object and LSF reconstruction of two metallic cylinders of diameter 0.4 cm aligned vertically with separation 3.2 cm.

problems associated with CW algorithms that use only a few discrete frequencies to

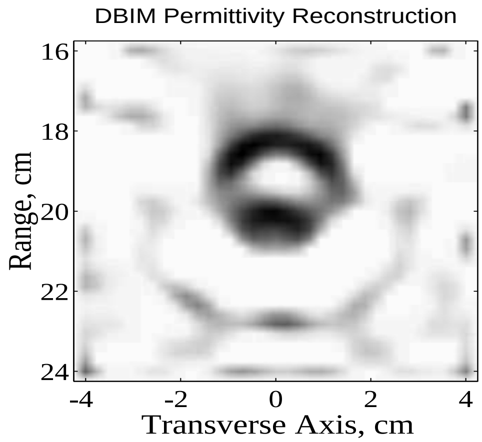


**Figure 15.** Reconstruction of microwave data from a hollow PVC pipe of diameter 2.7 cm in air.

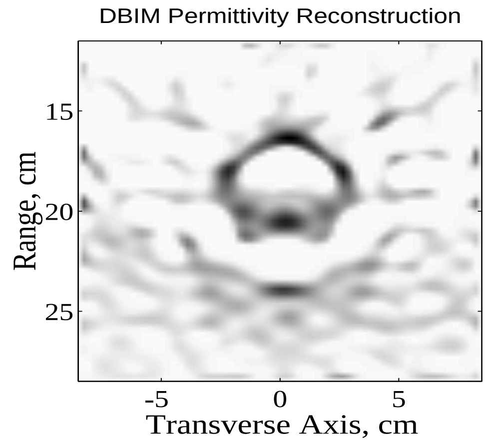


**Figure 16.** Reconstruction of microwave data from a hollow PVC pipe of diameter 4.8 cm in air.

generate a reconstruction. The BIM and DBIM were shown to perform well for dielectric objects, and the LSF method was shown to give a high-quality reconstruction for metallic objects.

Although we have achieved some very promising results thus far, there is still much work to be done in inverse scattering theory, developing better inversion algorithms, and improving data collection technology. The nonlinear inverse scattering algorithms presented here are capable of achieving much higher resolution and avoid many of the problems associated with previous methods such as computed tomography and diffraction tomography. However, most inverse scattering work that is currently being done deals with 2-D objects only. Future inverse scattering algorithms should be able to generate 3-D reconstructions if we are to remove modelling errors associated with using a 2-D model to approximate 3-D measurements. Work in the area of fast scattering solvers will also allow us to solve much larger inverse scattering problems.

## ACKNOWLEDGEMENTS

This work is supported by the Office of Naval Research under grant N000-14-89-J1286, the Army Research Office under contract DAAL03-91-G-0339, and the National Science Foundation under grant NSF-ECS-92-24466. Computer time is provided by the National Center for Supercomputer Applications at the University of Illinois, Urbana-Champaign.

## REFERENCES

1. W. C. Chew, *Waves and Fields in Inhomogeneous Media*: Van Nostrand Reinhold, 1990.
2. A. C. Kak, “Computerized tomography with X-ray, emission, and ultrasound sources,” *Proc. IEEE*, vol. 67, no. 9, pp. 1245–1272, 1979.
3. A. J. Devaney, “A filtered backpropagation algorithm for diffraction tomography,” *Ultrasonic Imaging*, vol. 4, pp. 336– 360, 1982.
4. D. Colton and P. Monk, “The inverse scattering problem for time harmonic acoustic waves in an inhomogeneous medium,” *Quart. J. Mech. Appl. Math.*, vol. 41, pp. 97–125, 1988.
5. T. S. Angell, R. E. Kleinman, and G. F. Roach, “An inverse transmission problem for the Helmholtz equation,” *Inverse Problems*, vol. 3, pp. 149–180, 1987.

6. T. M. Habashy and R. Mittra, "On some inverse methods in electromagnetics," *J. Electromag. Waves Appl.*, vol. 1, pp. 25–28, 1987.
7. J. -Ch. Bolomey, Ch. Durix, and D. Lesselier, "Determination of conductivity profiles by time-domain reflectometry," *IEEE Trans. Antennas Propagat.*, vol. AP–27, pp. 244–248, 1979.
8. S. A. Johnson and M. L. Tracy, "Inverse scattering solutions by a sinc basis, multiple source, moment method—part I: theory," *Ultrasonic Imaging*, vol. 5, pp. 361–375, 1983.
9. S. A. Johnson and M. L. Tracy, "Inverse scattering solutions by a sinc basis, multiple source, moment method—part II: numerical evaluations," *Ultrasonic Imaging*, vol. 5, pp. 376–392, 1983.
10. T. J. Cavicchi and W. D. O'Brien, "Numerical study of high-order diffraction tomography via the sinc basis moment method," *Ultrasonic Imaging*, vol. 11, pp. 42–74, 1989.
11. R. E. Kleinman and P. M. van den Berg, "Nonlinearized approach to profile inversion," *Int. J. Imag. Sys. Tech.*, vol. 2, pp. 119–126, 1990.
12. J. -Ch. Bolomey and Ch. Pichot, "Microwave tomography: from theory to practical imaging systems," *Int. J. Imag. Sys. Tech.*, vol. 2, pp. 144–156, 1990.
13. A. Tarantola, "The seismic reflection inverse problem," in *Inverse problems of acoustic and elastic waves*, F. Santosa, Y. H. Pao, W. Symes, and C. Holland, Eds.: Soc. Industr. Appl. Math., 1984.
14. E. Crase A. Pica, M. Noble, J. McDonald, and A. Tarantola, "Robust nonlinear waveform inversion: Application to real data," *Geophysics*, vol. 55, no. 5, pp. 527–538, 1990.
15. P. Mora, "Nonlinear two-dimensional elastic inversion of multioffset seismic data," *Geophysics*, vol. 52, no. 9, pp. 1211–1228, 1987.
16. N. Joachimowicz, Ch. Pichot, and J.-P. Hugonin, "Inverse scattering: An iterative numerical method for electromagnetic imaging," *IEEE Trans. Antennas Propagat.*, vol. AP–39, no. 12, pp. 1742-1752, December 1991.
17. W. C. Chew and S. L. Chuang, "Profile inversion of a planar medium with a line source or a point source," presented at *IGARSS, IEEE*, Strasbourg, France, 1984.
18. T. M. Habashy, W. C. Chew, and E. Y. Chow, "Simultaneous reconstruction of permittivity and conductivity profiles in a radially inhomogeneous slab," *Radio Sci.*, vol. 21, no. 4, pp. 635–645, 1986.
19. Y. M. Wang and W. C. Chew, "An iterative solution of the two-dimensional electromagnetic inverse scattering problem," *Int. J. Imag. Sys. Tech.*, vol. 1, pp.100–108, 1989.
20. W. C. Chew and Y. M. Wang, "Reconstruction of two-dimensional permittivity distribution using the distorted Born iterative method," *IEEE Trans. Medical Imag.*, vol. 9, no. 2, pp. 218–225, 1990.
21. Y. M. Wang and W. C. Chew, "Limited angle inverse scattering problems and their applications for geophysical explorations," *Int. J. Imag. Sys. Tech.*, vol. 2, no. 2, pp. 96–111, 1990.
22. M. Moghaddam and W. C. Chew, "Nonlinear two-dimensional velocity profile inversion in the time domain," *IEEE Trans. Geosci. Remote Sensing*, vol. GE–30, no. 1, pp. 147–156, Jan 1992.
23. Y. M. Wang and W. C. Chew, "Accelerating the iterative inverse scattering algorithms by using the fast recursive operator algorithm," *Radio Sci.*, vol. 27, no. 2, pp. March–April 1992.
24. M. Moghaddam, W. C. Chew, and M. Oristaglio, "Comparison of the Born iterative method and Tarantola's method for an electromagnetic time-domain inverse problem," *Int. J. Imag. Sys. Tech.*, vol. 3, no. 4, pp. 318–333, 1991.
25. M. Moghaddam and W. C. Chew, "Study of some practical issues in inversion with the Born iterative method using time-domain data," *IEEE Trans. Antennas*

*Propagat.*, vol. AP– 41, no. 2, pp. 177–184, 1993.

26. W. C. Chew and G. P. Otto, "Microwave imaging of multiple metallic cylinders using shape functions," *Micro. Guided Wave Lett.*, vol. 2, no. 7, pp. 284–286, 1992.
27. G. P. Otto and W. C. Chew, "Microwave inverse scattering—local shape function (LSF) imaging for improved resolution of strong scatterers," *IEEE Trans. Microwave Theory Tech.*, vol. MTT– 42, no. 1, pp. 137–141, 1994.
28. G. P. Otto and W. C. Chew, "Inverse scattering of $H_z$ waves using local shape function imaging: A T-matrix formulation," *Int. J. Imag. Sys. Tech.*, accepted for publication.
29. W. H. Weedon and W. C. Chew, "Time-domain inverse scattering using the local shape function (LSF) method," *J. Inverse Problems*, vol. 9, pp. 551–564, 1993.
30. W. H. Weedon and W. C. Chew, "Broadband microwave inverse scattering for nondestructive evaluation (NDE)," *Quantitative Nondestructive Evaluation Conference,* Bowdoin College, Maine, 1993.
31. D. T. Borup, S. A. Johnson, W. W. Kim, and M. J. Berggren, "Nonperturbative diffraction tomography via Gauss-Newton iteration applied to the scattering integral equation," *Ultrasonic Imaging*, vol. 14, pp. 69-85, 1992.
32. J. H. Lin, C. C. Lu, Y. M. Wang, W. C. Chew, J. J. Mallorqui, A. Broquetas, Ch. Pichot and J.-Ch. Bolomey, "Processing microwave experimental data with the distorted Born iterative method of nonlinear inverse scattering," *IEEE Antennas and Propagation Society International Symposium Digest*-vol. 1, pp. 500-503, June 28-July 2, University of Michigan, Ann Arbor, Michigan, 1993.
33. A. Taflove and M. E. Brodwin, "Numerical solution of steady-state electromagnetic scattering problems using the time-dependent Maxwell's equations," *IEEE Trans. Microwave Theory Tech.*, vol. MTT–23, pp. 623–630, 1975.
34. M. Born and E. Wolf, *Principles of Optics*, Pergamon Press, New York, First Edition, 1959, Sixth Edition, 1980.